 doi:10.20944/preprints202204.0058.v1

Assessment of PVS enhancement methods using a three-dimensional computational model

Jose Bernal[1], Maria d. C. Valdés-Hernández[1,3,*], Javier Escudero[2], Roberto Duarte[1], Lucia Ballerini[1], Mark E. Bastin[1,3], Ian J. Deary[3], Michael J. Thrippleton[1], Rhian M. Touyz[4], and Joanna M. Wardlaw[1,3]

[1] Centre for Clinical Brain Sciences, The University of Edinburgh, Edinburgh, UK
[2] Institute for Digital Communications, The University of Edinburgh, Edinburgh, UK
[3] Lothian Birth Cohorts group, Department of Psychology, The University of Edinburgh, UK
[4] Research Institute of the McGill University Health Centre, McGill University, Montréal, Canada
* Corresponding author

Abstract

Growing interest surrounds the assessment of perivascular spaces (PVS) on magnetic resonance imaging (MRI) and their validation as a clinical biomarker of adverse brain health. Nonetheless, the limits of validity of current state-of-the-art segmentation methods is still unclear. Here, we propose an open-source computational model generating three-dimensional digital reference objects to evaluate enhancement performance in relation to PVS characteristics and spatiotemporal imaging considerations (including sampling, motion artefacts, and Rician noise). With it, we study the performance of the Frangi, Jerman and RORPO filters in enhancing PVS-like structures to facilitate segmentation. Our findings were three-fold. First, as long as voxels are isotropic, RORPO outperforms all other filters, regardless of imaging quality. Unlike the Frangi and Jerman filters, RORPO's performance does not deteriorate as PVS volume increases. Second, the performance of all "vesselness" enhancement filters is heavily influenced by imaging quality, with sampling and motion artefacts being the most damaging for these types of analyses. Third, none of the filters can distinguish PVS from other hyperintense structures (e.g. white matter hyperintensities, stroke lesions, or lacunes) effectively, the area under precision-recall curve dropped substantially (Frangi: from 94.21 [IQR 91.60, 96.16] to 43.76 [IQR 25.19, 63.38]; Jerman: from 94.51 [IQR 91.90, 95.37] to 58.00 [IQR 35.68, 64.87]; RORPO: from 98.72 [IQR 95.37, 98.96] to 71.87 [IQR 57.21, 76.63] without and with other hyperintense structures, respectively). The use of our computational model enables comparing segmentation methods and identifying their advantages and disadvantages, thereby providing means for testing and optimising pipelines for ongoing and future studies.

 doi:10.20944/preprints202204.0058.v1

Keywords

Digital reference object; Perivascular spaces; Spatio-temporal imaging artefacts; Perivascular space enhancement; Cerebral small vessel disease

1. Introduction

Perivascular spaces (PVS) in the brain are small fluid-filled tubular structures that surround cerebral microvessels usually less than 3mm max diam (Wardlaw et al., 2020). As part of the brain fluid exchange, or glymphatic system, these are thought to play an essential role in waste elimination, interstitial fluid exchange, and, more broadly, in maintaining healthy brain function (Wardlaw et al., 2020). If enlarged or dilated, PVS become visible on structural magnetic resonance imaging (MRI) (Wardlaw et al., 2020). Even though a few visible PVS may be normal at any age, their abundance and enlargement are associated with ageing, hypertension, altered BBB permeability (Li et al., 2018), and other neuroimaging features of small vessel disease (SVD) (Francis et al., 2019). Accurate quantification of PVS is therefore crucial to determine their involvements in SVD and in the nervous system in a broader context.

The evolution of neuroradiological imaging technologies has enabled visualising enlarged PVS. Quantification for research purposes has, until recently, relied primarily on clinical visual scores (Heier et al., 1987; Patankar et al., 2005; Potter et al., 2015; Rouhl et al., 2008), which approximate the frequency of PVS in several standard brain regions according to ordinal scales (Ballerini et al., 2018). However, the ordinal visual scales are relatively insensitive, may be prone to variation between observers, especially when co-occurring with other SVD features (González-Castro et al., 2017), and do not capture other aspects of PVS such as length, width, individual or total PVS volumes.

The use of computational techniques could help to overcome the limitations of visual scores if accurate, and reduce operator time and subjectivity. However, computational quantification of subtle neuroimaging features such as small visible PVS (i.e., albeit in a macroscopic scale) is extremely challenging due to the small size, the frequency of artefacts, and substandard processing workflows (Ballerini et al., 2020b, 2018). Additionally, from a computational perspective, two additional issues limit their translation to clinics:

- **Proposal validation and lack of a ground truth**: the development of computational processing techniques requires a ground truth, e.g. clinically validated segmentation of the structures of interest. Nonetheless, building a ground truth for PVS is an extremely time-consuming, laborious, and impractical task to perform, especially on a large scale and when dealing with abundant

Preprints (www.preprints.org) | NOT PEER-REVIEWED | Posted: 7 April 2022 doi:10.20944/preprints202204.0058.v1

structures of small size. Moreover, validation of a few techniques may require correlating *in vivo* and *ex vivo* observations, making it impractical in real life.

- **Subtlety and imaging artefacts**: imaging artefacts arising during MRI scanning can compromise the quantification of subtle neuroimaging features. Although compensating for these visual distortions retrospectively may seem useful, careful testing and tuning is essential to avoid accidentally removing clinically relevant information.

Computational techniques that rely on explicit geometrical information often consider three major steps: pre-processing, PVS enhancement, and segmentation (Ballerini et al., 2020a, 2018; Bernal et al., 2021b; Liu et al., 2020; Ramirez et al., 2015; Sepehrband et al., 2021, 2019; Valdés Hernández et al., 2020; Wang et al., 2016). At first, all images undergo quality control, inter- or intra-scan intensity standardisation, spatial normalisation, or noise reduction. Then, researchers employ "vesselness" enhancement methods to increase the saliency of tubular structures (including PVS). Lastly, binarisation of "vesselness" response maps, segmentation mask refinement, and connected component analysis take place. In this paper, we specifically evaluate the performance and robustness of "vesselness" enhancement methods. We scrutinise their behaviour in the presence of typical imaging distortions caused by sampling, motion artefacts, and noise, as well as other pathological features that may co-occur. For this purpose, we propose an open-source computational model that synthesises three-dimensional T2-weighted-like images with PVS-like structures distributed throughout the brain.

2. Materials and methods

Our computational model works as illustrated in Figure 1 and described in the following sections.

Preprints (www.preprints.org) | NOT PEER-REVIEWED | Posted: 7 April 2022 doi:10.20944/preprints202204.0058.v1

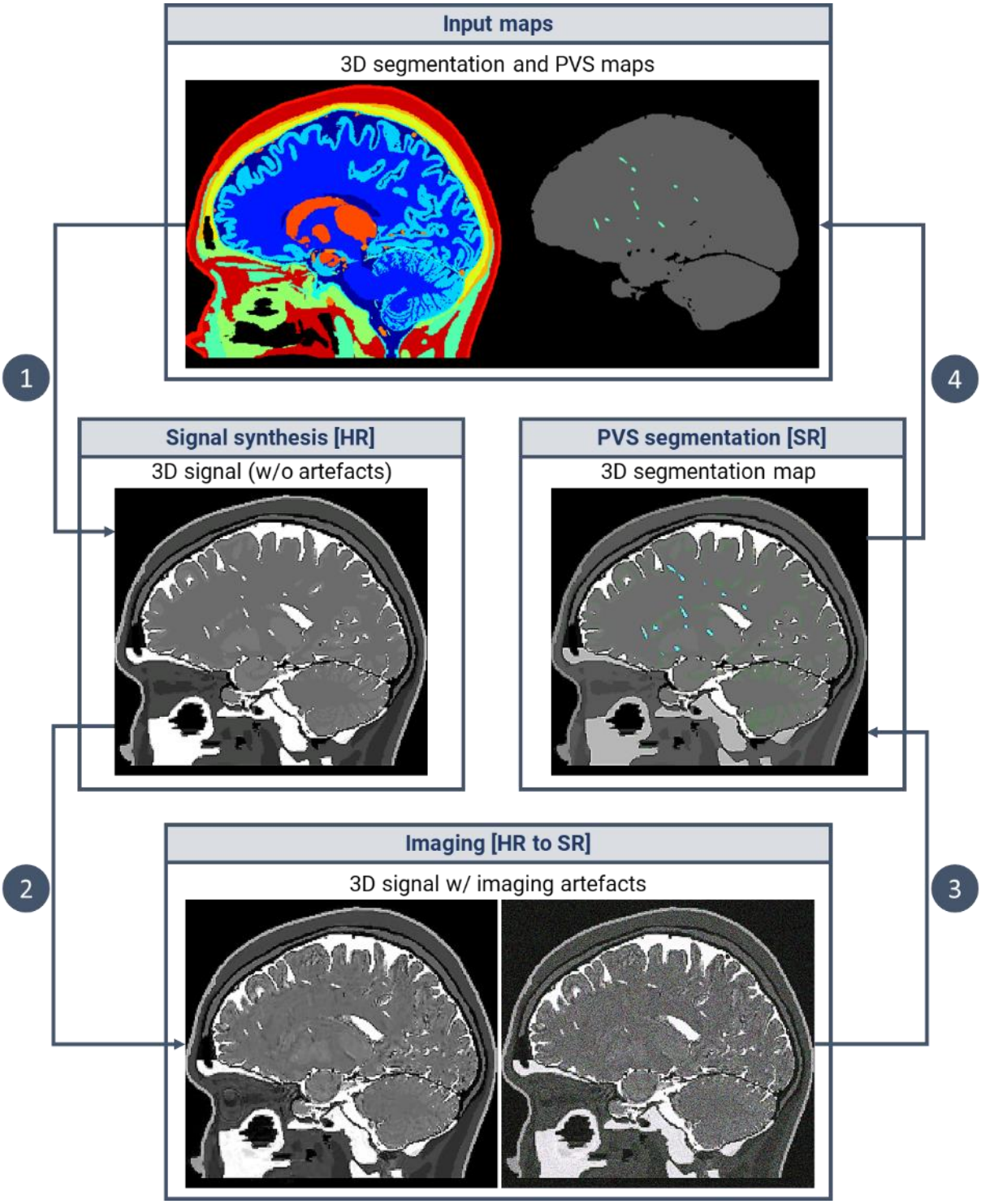

Figure 1. Computational model for assessing PVS quantification. We generate maps with PVS-like structures in different orientations and locations throughout the brain. We use a high-resolution model of the head and the resulting "PVS" maps to synthesise T2-weighted like images. We then sample these high-resolution digital reference objects (DRO) and incorporate motion and Rician noise to generate the "acquired" T2-weighted image. We finally segment the "PVS" on this DRO and compare the results against the ground truth. The closer the results to the ground truth, the more resilient the "vesselness" enhancement method against distortion. HR: high-resolution. SR: scanning resolution.

Preprints (www.preprints.org) | NOT PEER-REVIEWED | Posted: 7 April 2022 doi:10.20944/preprints202204.0058.v1

2.1 Computational model

2.1.1 Reference head model

We leveraged on the MIDA model, a three-dimensional 0.5×0.5×0.5-mm human head and neck atlas of a healthy volunteer (Iacono et al., 2015)[1]. This publicly available digital model contains the segmentation of 116 cerebral and non-cerebral structures. We excluded extra-cerebral regions and combined some others to reduce the level of granularity and focus on those of interest: normal-appearing white matter, cortical and subcortical grey matter, and cerebrospinal fluid (Figure 2).

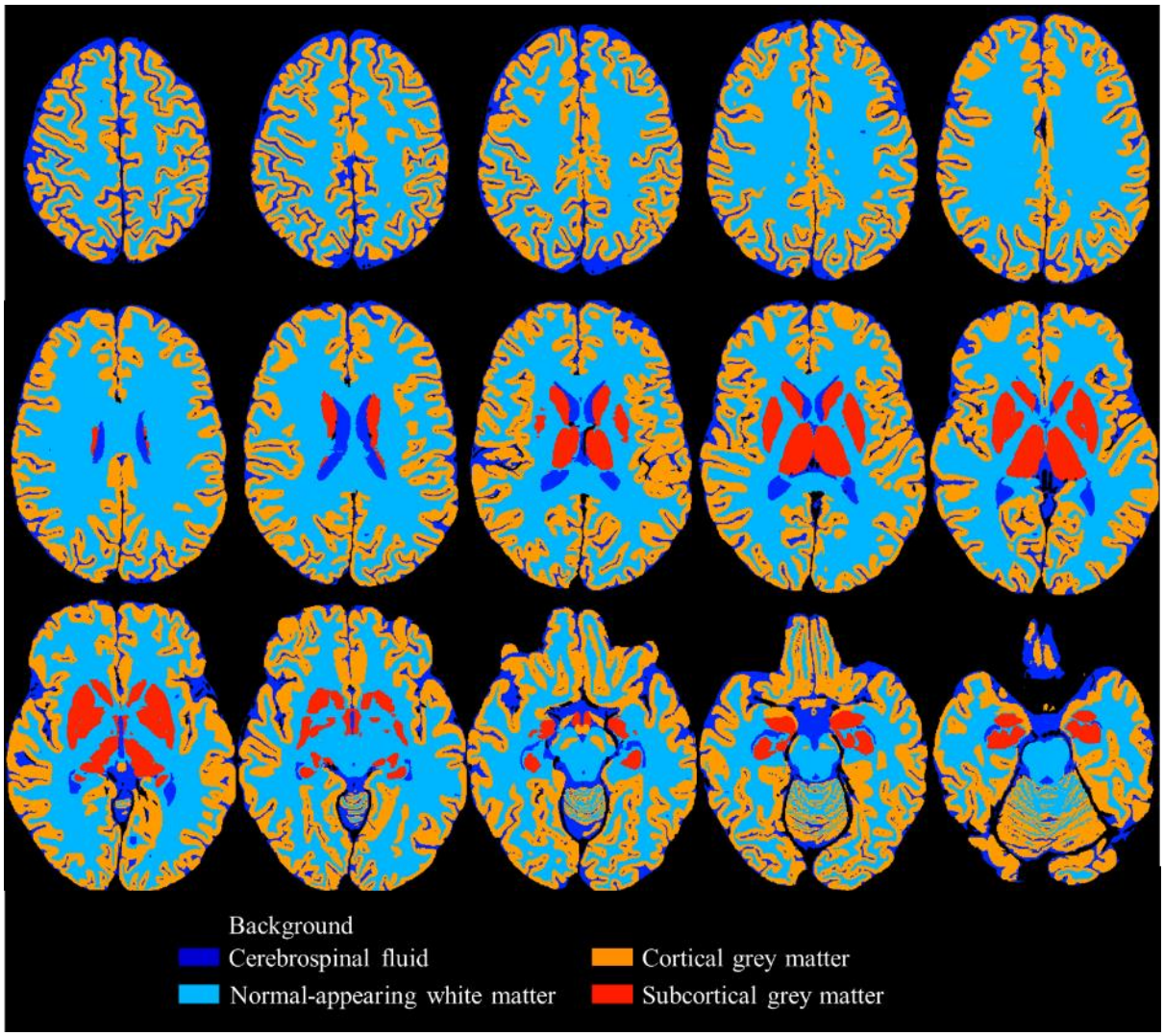

Figure 2. Brain model of reference. In total, we considered five healthy regions of interest: normal-appearing white matter, cortical and subcortical grey matter, and cerebrospinal fluid. We do not synthesise PVS in the cerebellum.

[1] The MIDA human head model can be downloaded from *www.itis.ethz.ch/MIDA/*

Preprints (www.preprints.org) | NOT PEER-REVIEWED | Posted: 7 April 2022 doi:10.20944/preprints202204.0058.v1

Pathological regions

The presence of white matter hyperintensities (WMH) near or around PVS may influence the ability of enhancement filters to highlight PVS appropriately. Thus, in a few experiments, we synthesised them using spatial occurrence templates extracted from patient data (https://doi.org/10.7488/ds/2716).

2.1.2 PVS model

Clinical publications describe PVS as tiny tubular structures in the brain (Wardlaw et al., 2020). Thus, we modelled PVS as cylinders using the following equations: $x^2 + y^2 \leq r^2$ and $z \leq h$, where $2r$ and h represent the width and height of a PVS, $r, h \in \mathbb{R}^+$. The volume of each PVS is consequently equal to $\pi r^2 h$. We synthesised these structures in the three regions where they are often seen: centrum semiovale, basal ganglia, and pontomesencephalic junction (Wardlaw et al., 2020).

2.1.3 Simulation of acquired data and motion effects

We leveraged a recent, open-source, and publicly-available four-dimensional computational model to simulate MRI data acquisition (Bernal et al., 2021a).

k-space sampling

We calculated the *k*-space representation of the high-resolution DRO as the three-dimensional inverse Fourier transform. We resampled it to obtain *k*-space data with the acquired field of view and spatial resolution. We assumed three-dimensional Cartesian *k*-space sampling. To emulate band filtering and slab-selective excitation, we suppressed signals from outside the field of view in the frequency- and slice-encoding directions. Finite *k*-space sampling results in information loss, visually manifesting in Gibbs ringing artefacts and partial volume effects.

Motion artefacts

Ghosting, blurring or ringing caused by motion affect the visual quality of the MRI scans, potentially compromising the quantification of subtle neuroimaging features. We studied their effect on PVS quantification using a composite *k*-space model (Bernal et al., 2021a; Shaw et al., 2020): we extract random proportions of successive *k*-space lines with the head on different positions and put them together to create a composite *k*-space (Figure 3). We generated three head positions by rotating the DRO random angles (±2.5° for rotations).

Preprints (www.preprints.org) | NOT PEER-REVIEWED | Posted: 7 April 2022 doi:10.20944/preprints202204.0058.v1

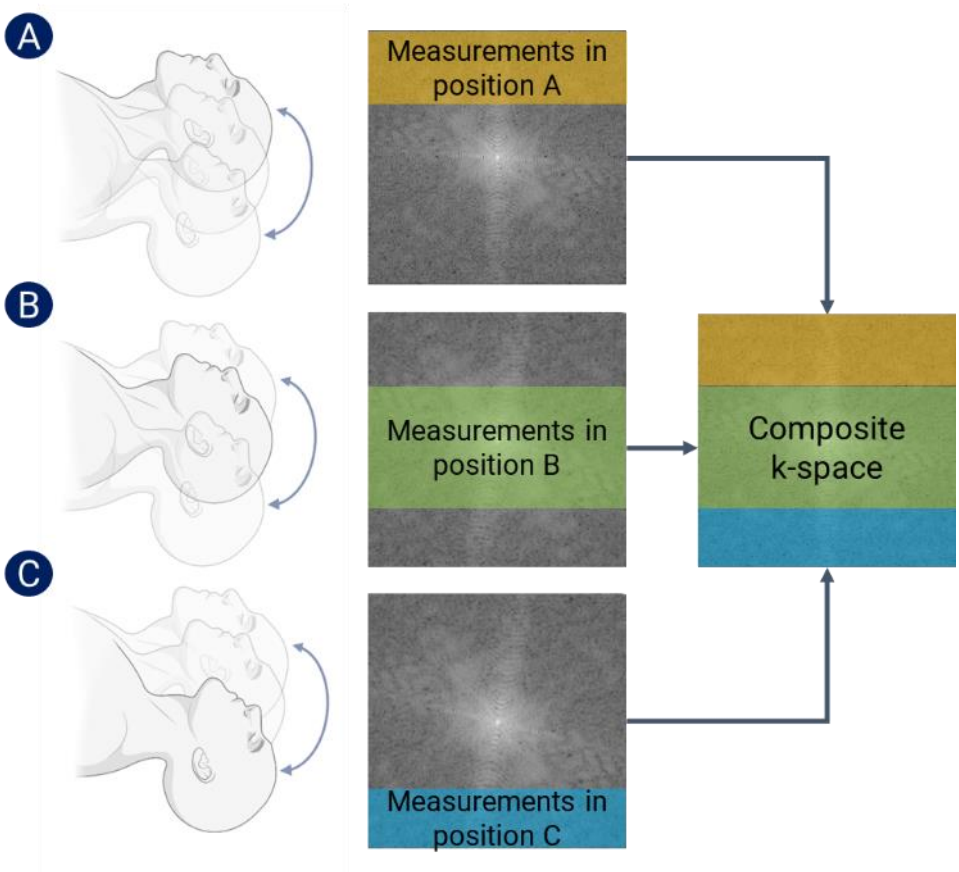

Figure 3. Simulation of motion artefacts. We simulate motion artefacts by generating composite k-spaces: we take random portions of successive k-space lines from position A, B, and C. Created in part with BioRender.com

Rician noise

The signal-to-noise ratio may reduce the performance of the PVS enhancement filter. We investigated the effect of Rician noise by adding uncorrelated additive white Gaussian noise to the real and imaginary channels of the *k*-space data. We then use the three-dimensional Fourier transform and computed the magnitude to yield the DRO image, now including sampling artefacts, motion artefacts, and Rician noise.

2.2 In-silico experiments

2.2.1 MR protocol parameters and intensity data for generating DROs

We retrieved intensity data from the T2-weighted (T2-w) brain MRI scans of the Lothian Birth Cohort 1936 (LBC1936) study, a large-scale study from 700 community-dwelling individuals (mean age 72.6 [SD 0.7]; 48.3% female; estimated intensities in Table 1). Data from this study has already been used to demonstrate meaningful and sensitive relations between computational PVS measurements and WMH burden and risk factors (Ballerini et al., 2020a, 2020b). Written informed consent was obtained

Preprints (www.preprints.org) | NOT PEER-REVIEWED | Posted: 7 April 2022 doi:10.20944/preprints202204.0058.v1

from each participant under protocols approved by the Lothian (REC 07/MRE00/58) and Scottish Multicentre (MREC/01/0/56) Research Ethics Committees (http://www.lothianbirthcohort.ed.ac.uk/) (Deary et al., 2007).

Structural MRI scans were obtained using a 1.5-Tesla GE Signa Horizon HDx scanner (General Electric, Milwaukee, WI) and the T2-w sequences were acquired with the following parameters: 11320 ms repetition time, 104.9 ms echo time, 20.83 kHz bandwidth, 2 mm slice thickness, and 256 × 256 mm field-of-view. All images were first resampled to a 256 × 256 × 80 matrix, 1 mm in-plane resolution. PVS in the normal-appearing white matter were segmented on T2-w MRI using a thoroughly validated method leveraging the Frangi filter to enhance them (Ballerini et al., 2020a, 2018). In addition, after segmentation, an experienced image analyst visually inspected all binary segmentation masks to remove erroneous ones. Images were considered acceptable if the method detected a reasonable amount of visible PVS and did not flag too many artefacts as potential PVS candidates (< 20% of false positives and false negatives). Around 77% (n=540) of segmentation masks passed this test (Ballerini et al., 2020a).

Table 1. Absolute signal intensities. We retrieved these values from the Lothian Birth Cohort 1936 study (Ballerini et al., 2020a). We also present signal intensity variations between perivascular spaces and other regions of interest (ROI) as a measure of contrast (i.e. $100 * (\text{Intensity}_{\text{ROI}}/\text{Intensity}_{\text{PVS}} - 1)$*). We report mean and standard deviation.*

Region of interest	Signal intensity	$100 * \left(\frac{\text{Intensity}_{\text{ROI}}}{\text{Intensity}_{\text{PVS}}} - 1\right)$
Cerebrospinal fluid	1152.03 (236.69)	110.41 (59.59)
Normal-appearing white matter	395.54 (69.86)	-27.76 (19.00)
White matter hyperintensity	657.27 (118.05)	20.04 (31.82)
Grey matter	450.02 (82.09)	-17.80 (21.94)
Perivascular spaces	547.52 (106.74)	0.00 (0.00)

2.2.2 Experiments

We generated high-resolution T2-w like DROs with PVS of different sizes distributed all over the brain. The length of each PVS ranged from 0.5 to 10 mm and their width from 0.5 to 3 mm. We considered three main aspects of interest. First, we tested all three enhancement filters on these ideal high quality high-resolution DROs to determine whether their performance varied with PVS dimensions. Second, we performed *in-silico* experiments to investigate the impact of k-space sampling, motion artefacts, and Rician noise on enhancement results. Third, we synthesised DROs with "WMH" to study whether

Preprints (www.preprints.org) | NOT PEER-REVIEWED | Posted: 7 April 2022 doi:10.20944/preprints202204.0058.v1

enhancement filters were able to discern between tubular and non-tubular hyperintense structures. We ran each combination (aspect of interest, PVS length, PVS width). We repeated each experiment ten times and reported mean and standard deviation (RStudio v1.2.5019 with R v3.5.1). We ran all experiments on a 189GB RAM computer running Scientific Linux 7.3 (Nitrogen; Arch x86 64; 56 CPUs Intel(R) Xeon(R) CPU E5-2683 v3 @ 2.00GHz).

2.3 "Vesselness" enhancement methods

2.3.1 Hessian-based enhancement methods

The majority of PVS enhancement approaches rely on the analysis of the second-order derivatives, which encode geometric properties, to separate tubular structures from round or planar ones (Frangi et al., 1998; Jerman et al., 2015; Lamy et al., 2020).

In a nutshell, the functioning of Hessian-based filters consists of three main steps (Lamy et al., 2020). First, second-order partial derivatives are computed for each voxel to form the Hessian matrix H, i.e. $(Hf)_{ij} = {\partial^2 f}/{\partial x_i \partial x_j}$. Given that the computation of H requires the function to be continuous and twice differentiable, digital images are often convolved with Gaussian kernels in advance. Second, the eigenvalues of the Hessian matrix are found. The sign and magnitude of these eigenvalues $\lambda_1, \lambda_2, \lambda_3$, with $|\lambda_1| \leq |\lambda_2| \leq |\lambda_3|$, are indicative of whether a voxel contains a bright structure and whether it is tubular. The search for PVS can be narrowed down to regions fulfilling $|\lambda_1| \approx 0$ and $\lambda_2 \approx \lambda_3 \ll 0$, as these constraints limit responses to hyperintense tubular structures (Lamy et al., 2020). Third, further analysis of eigenvalues enables filtering potential candidates by specific properties, such as contrast and eccentricity. The Frangi and Jerman filters present two approaches for improved detection of elongated structures.

2.3.1.1 The Frangi filter

The Frangi filter (Frangi et al., 1998) — considered by many the gold standard of Hessian-based filtering (Lamy et al., 2020) — examines three additional properties $R_b = |\lambda_1|/\sqrt{|\lambda_2 \lambda_3|}$, $R_a = |\lambda_2|/|\lambda_3|$, and $S = \sqrt{\lambda_1^2 + \lambda_2^2 + \lambda_3^2}$ to filter blobs, lines, and low contrast structures, respectively (Frangi et al., 1998; Lamy et al., 2020). These three aspects are jointly evaluated in the following likelihood response:

$$V = \begin{cases} 0 \text{ if } \lambda_2 > 0 \text{ or } \lambda_3 > 0, \\ \left(1 - e^{-R_a^2/2a^2}\right) \cdot \left(e^{-R_b^2/2b^2}\right) \cdot \left(1 - e^{-S^2/2c^2}\right) \text{ otherwise,} \end{cases} \quad (1)$$

and the sensitivity of the filter to each of them is adjusted via a, b, and $c \in \mathbb{R}^+$.

Preprints (www.preprints.org) | NOT PEER-REVIEWED | Posted: 7 April 2022 doi:10.20944/preprints202204.0058.v1

We use the implementation of the Frangi filter available in MathWorks (www.mathworks.com/matlabcentral/fileexchange/24409-hessian-based-frangi-vesselness-filter).

2.3.1.2 The Jerman filter

The Jerman filter (Jerman et al., 2015) is also a Hessian-based filter. This filter takes inspiration from the volume ratio, a scalar index used in diffusion tensor imaging to gauge structural anisotropy (Pierpaoli and Basser, 1996; Vilanova et al., 2006). The likelihood response of the Jerman filter is the following:

$$V = \begin{cases} 0 \text{ if } \lambda_2 > 0 \text{ or } \lambda_3 > 0, \\ \lambda_2^2 \cdot (\lambda_3^* - \lambda_2) \cdot \left(\frac{3}{\lambda_2 + \lambda_3^*}\right)^3 \text{ if } \lambda_2 \leq 0.5 \cdot \lambda_3^*, \\ 1 \text{ otherwise,} \end{cases} \quad (2)$$

where λ_3^* is a regularised version of λ_3 which prevents division by zero.

We used the implementation available in MathWorks (www.mathworks.com/matlabcentral/fileexchange/63171-jerman-enhancement-filter).

2.3.2 Ranking Orientation Responses of Path Operators (RORPO)

Unlike the previous methods, RORPO does not rely on differential information, but on mathematical morphology, path opening in particular (Merveille et al., 2018, 2014). Given an input binary image $X: \mathbb{R}^3 \rightarrow \{0, 1\}$ and a connectivity operator Γ, path opening $\alpha_L^{\Gamma}(X)$ consists of finding all possible paths of length L in X (Heijmans et al., 2005), understanding "path" as a set of successively connected voxels according to Γ. RORPO utilises this notion of path opening to detect tubular structures in an eight-bit image $I: \mathbb{R}^3 \rightarrow \mathbb{R}$. First, it applies path opening in multiple directions using seven connectivity operators $\{\Gamma_i\}_{i\epsilon\,[1,7]}$. Since this operation applies to binary images, RORPO thresholds I on all possible intensity levels (e.g. $\tau \in [0, 2^8 - 1]$ for an eight-bit image). This step results in seven response images $\{A_L^{\Gamma_i}(I)\}_{i\epsilon\,[1,7]}$, where each $A_L^{\Gamma_i}(I) = \max_{\tau \in [0,2^8-1]} \{\tau | (x, y, z)\, \epsilon\, \alpha_L^{\Gamma_i}(I \geq \tau)\}$. Second, RORPO computes the difference between the maximum and median response for every voxel in $\{A_L^{\Gamma_i}(I)\}_{i\epsilon\,[1,7]}$. The higher the difference, the more likely a voxel pertains to a thin object rather than a blob since the response of an isotropic structure will be similar in all directions. This difference image is the output of the filter (Figure 4).

Preprints (www.preprints.org) | NOT PEER-REVIEWED | Posted: 7 April 2022 doi:10.20944/preprints202204.0058.v1

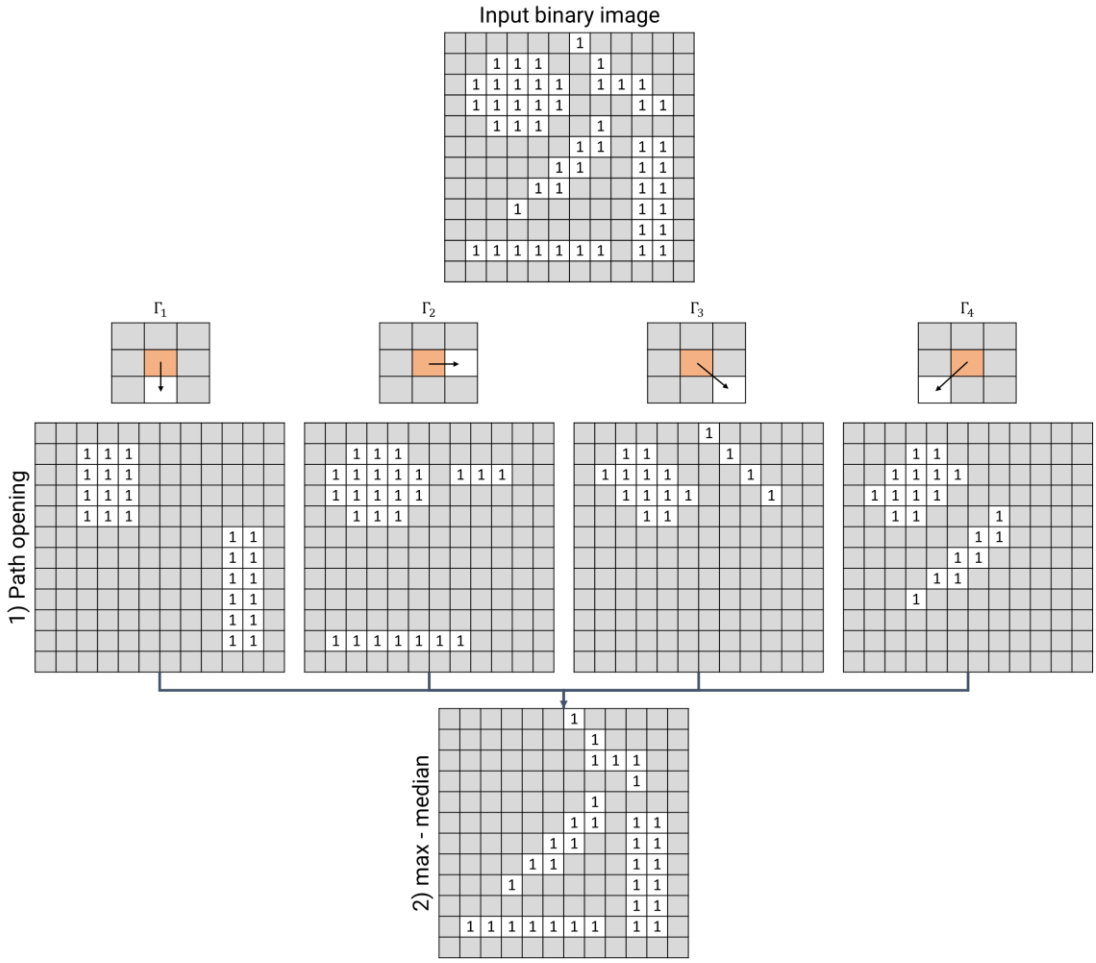

Figure 4. Illustration of the functioning of RORPO on a 2D binary image. First, RORPO applies path opening with connectivity operators $\Gamma_{i\in[1,n]}$ in n directions, leading to n response images. In this example, we assume $n = 4$ and the length of the path $L = 3$. Second, RORPO computes and outputs the difference between the maximum and median response for each voxel. A voxel remaining in all response images receives a value of zero (both the maximum and median response equal to one) whereas those in only one receive a value of one (maximum and median response equal to one and zero, respectively).

The parameter L, which controls the length of the paths, requires tuning depending on the problem at hand. However, since it has a physical meaning related to the length of the object of interest, it is easily adjustable. We applied the implementation of RORPO available in GitHub (https://github.com/path-openings/RORPO).

2.4 Performance metrics

We evaluated enhancement results using three metrics based on the confusion matrix, precision, recall, F-score, and the area under the precision-recall curve (AUPRC). We opted for precision-recall

Preprints (www.preprints.org) | NOT PEER-REVIEWED | Posted: 7 April 2022 doi:10.20944/preprints202204.0058.v1

curves instead of the popular receiver operating curves due to the dramatic disproportion between positive (i.e. PVS) and negative samples.

2.4.1 Precision

Precision allows us to examine the proportion of correctly segmented PVS. Given a binary segmentation map S and a binary ground truth GT, we computed precision by dividing the number of voxels classified as PVS in both images by the number of voxels classified as PVS in S, i.e.

$$\text{Precision} = \frac{\sum S \cap GT}{\sum S}. \quad (3)$$

The values for precision lay between zero and one, being one the maximum and best precision score a method can obtain.

2.4.2 Recall

Recall allows us to examine the proportion of PVS the filter actually identified. We computed recall by dividing the number of voxels classified as PVS in both images by the number of voxels classified as PVS in GT, i.e.

$$\text{Recall} = \frac{\sum S \cap GT}{\sum GT}. \quad (4)$$

The minimum and maximum recall scores are zero and one respectively.

2.4.3 Area under precision-recall curve (AUPRC)

The AUPRC summarises the precision and recall values obtained by the enhancement method for different thresholds applied on the filter response maps. We computed the AUPRC by integrating over the precision-recall curve. Consequently, a good PVS segmentation method should obtain AUPRC values close to one.

3. Results

3.1 Baseline performance

We first segmented the PVS-like structures on clean high-resolution images to measure the performance of all filters in the absence of distortion. We noticed PVS dimensions influenced enhancement effectiveness. First, RORPO outperformed both Hessian-based filters in most cases (AUPRC - RORPO: 98 [IQR 98, 99]; Frangi: 96 [IQR 95, 97]; Jerman: 96 [IQR 95, 97]), except when dealing with the smallest 1.0 × 0.5 or 1.5 × 0.5 mm PVS (AUPRC around 94.5 for RORPO vs ~100 for Frangi and Jerman). We noticed that RORPO produced low, partial, or null responses for PVS neighbouring the boundaries of the region of interest (Figure 5). Second, Hessian-based filters performed worse with increasing PVS volume; e.g. their AUPRC values were close to 100 for 3.5 × 2.0 mm PVS but 95 for 10.0

Preprints (www.preprints.org) | NOT PEER-REVIEWED | Posted: 7 April 2022 doi:10.20944/preprints202204.0058.v1

× 3.0 mm PVS. Inspection of filter response maps revealed that this outcome was a consequence of the poor localisation of Hessian-based filters – not only voxels comprising PVS but also those around them had a positive response (Figure 5).

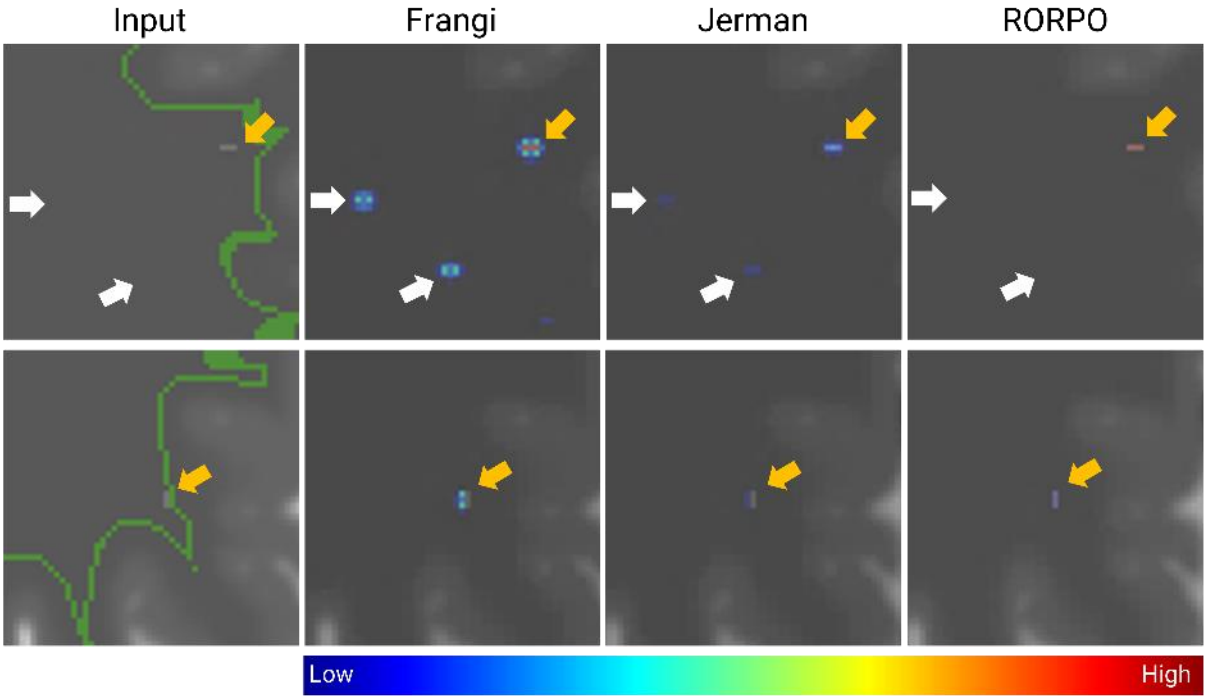

Figure 5. Filter response maps on clean 0.5 × 0.5 × 0.5 mm images. The green boundary in "Zoom" delimits the region of interest. Yellow arrows point to actual PVS-like structures (referred to as PVS for simplicity). In maps produced by the Frangi and Jerman filters, voxels around PVS have a non-zero response (white arrows). RORPO produces lower responses for PVS around boundaries of the region of interest (PVS appears red in top row vs blue in bottom row). Outputs cannot be compared between filters as values vary in range and scale.

3.2 Effect of imaging considerations

3.2.1 Slice thickness

We present DROs before and after *k*-space sampling to represent slice thickness of 0.5, 1, and 2 mm in Figure 6. Note the slice thickness of the real T2-w images used to derive the DRO is 2 mm. Thicker slices increased partial volume averaging effects, which in turn reduced PVS saliency and sharpness. Moreover, slice thickness prevents visibility in some cases: PVS of length lower than 2 mm or width lower than 1 mm were not visible at 1 × 1 × 1 and 1 × 1 × 2 mm resolutions.

Preprints (www.preprints.org) | NOT PEER-REVIEWED | Posted: 7 April 2022 doi:10.20944/preprints202204.0058.v1

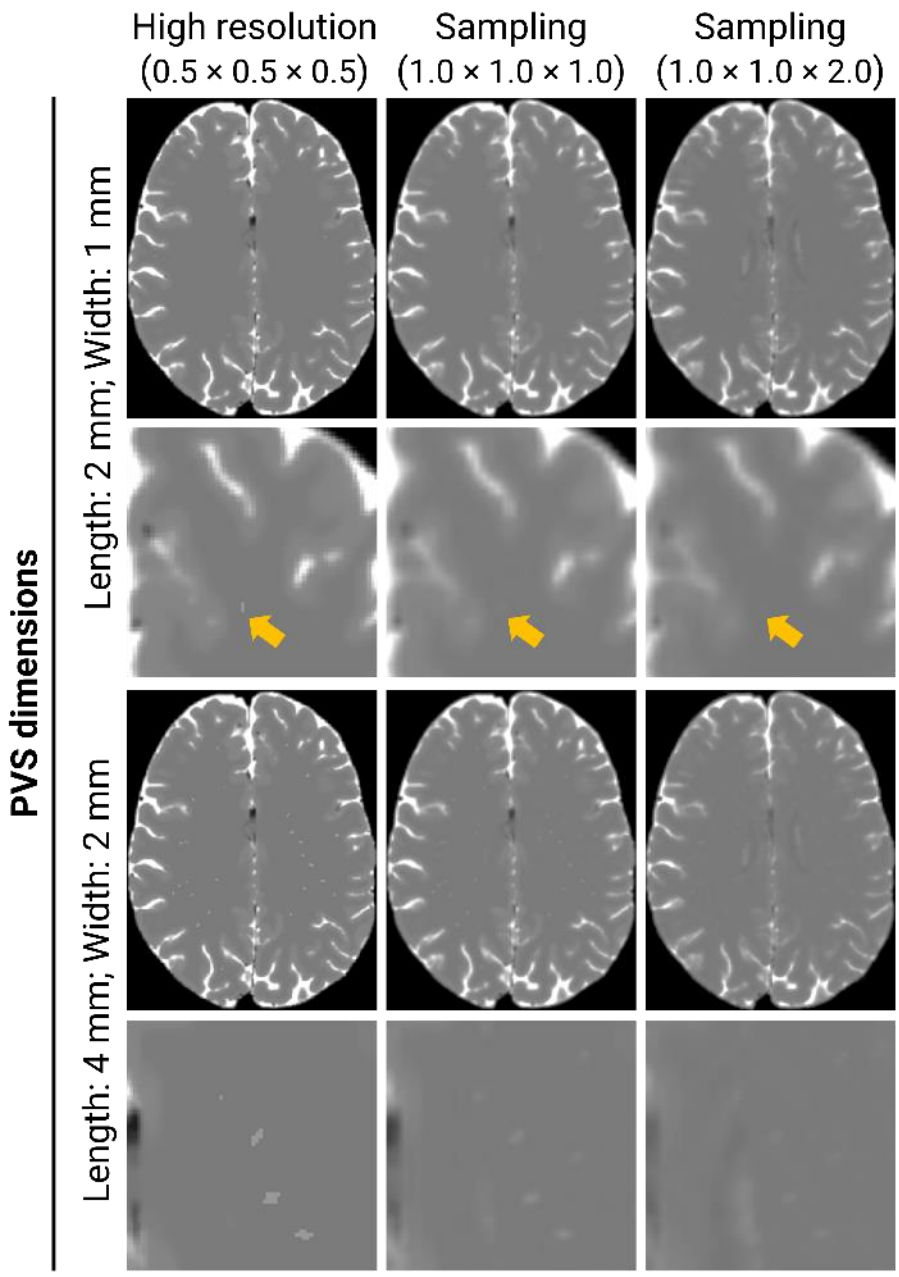

Figure 6. k-space sampling leads to partial volume averaging, which limit PVS visibility. This situation is particularly evident for 2-mm length and 1-mm width PVS (yellow arrow). Imaging considerations: k-space sampling.

We then segmented PVS on 1 × 1 × 1 and 1 × 1 × 2 mm images (Figure 7). Our findings were two-fold. First, both precision and recall decreased in thicker slices. For PVS of 4 mm length and 2 mm width, the maximum recall at the maximum precision in 1 × 1 × 1 mm resolution images was at least 30% (Frangi: 30%; Jerman: 30%; RORPO: 58%), whereas it was between 7% and 26% in 1 × 1 × 2 mm (Frangi: 7%; Jerman: 26%; RORPO: 14%) (Figure S1). Second, Gibbs ringing artefacts often exhibited a low but non-zero response (Figure 8), i.e. they may be incorrectly picked up depending on the threshold.

Preprints (www.preprints.org) | NOT PEER-REVIEWED | Posted: 7 April 2022 doi:10.20944/preprints202204.0058.v1

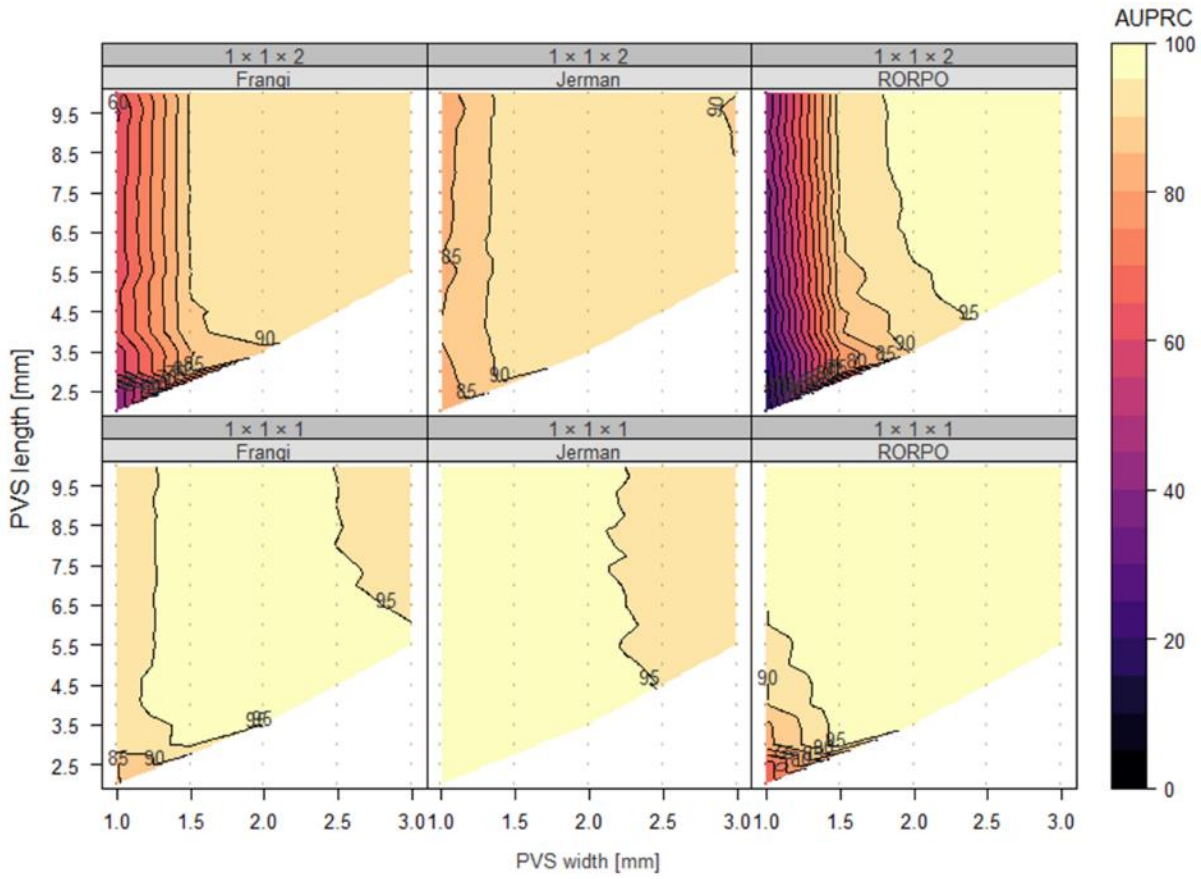

Figure 7. The performance of PVS enhancement filters decreases as slice thickness increases. We considered two scanning resolutions, 1 × 1 × 1 (bottom row) and 1 × 1 × 2 (top row) mm, to explore the impact of isotropic and anisotropic voxels on enhancement performance. White regions represent cases that were not considered (width >= length, eccentricity < 0.8, or lack of PVS visibility). Imaging considerations: k-space sampling.

Preprints (www.preprints.org) | NOT PEER-REVIEWED | Posted: 7 April 2022 doi:10.20944/preprints202204.0058.v1

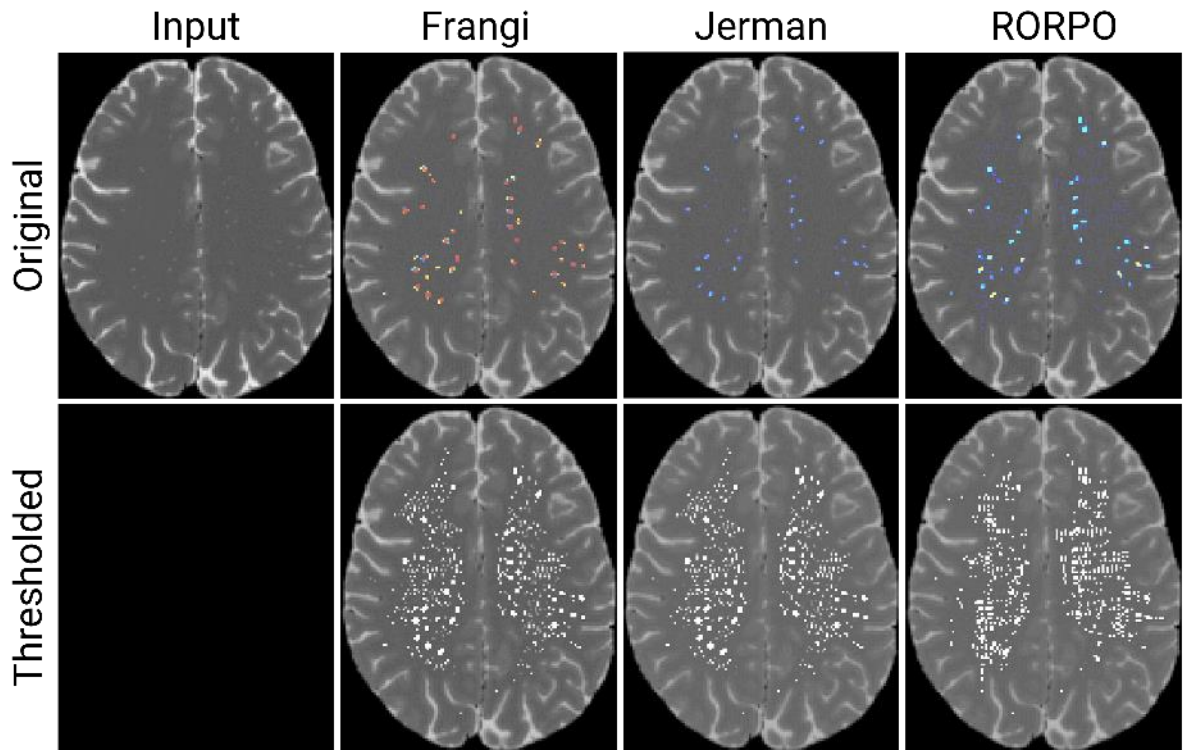

Figure 8. PVS enhancement filters pick up Gibbs ringing artefacts propagating from T2-w hyperintense regions (the non-zero response of ringing artefacts is visible in the bottom row). Imaging considerations: k-space sampling.

3.2.2 Motion artefacts

We used the composite *k*-space model to simulate motion artefacts (Figure 9). Our computational model produced ringing and ghosting artefacts, in alignment with the theory. Note PVS remained visible after inducing motion artefacts.

Preprints (www.preprints.org) | NOT PEER-REVIEWED | Posted: 7 April 2022 doi:10.20944/preprints202204.0058.v1

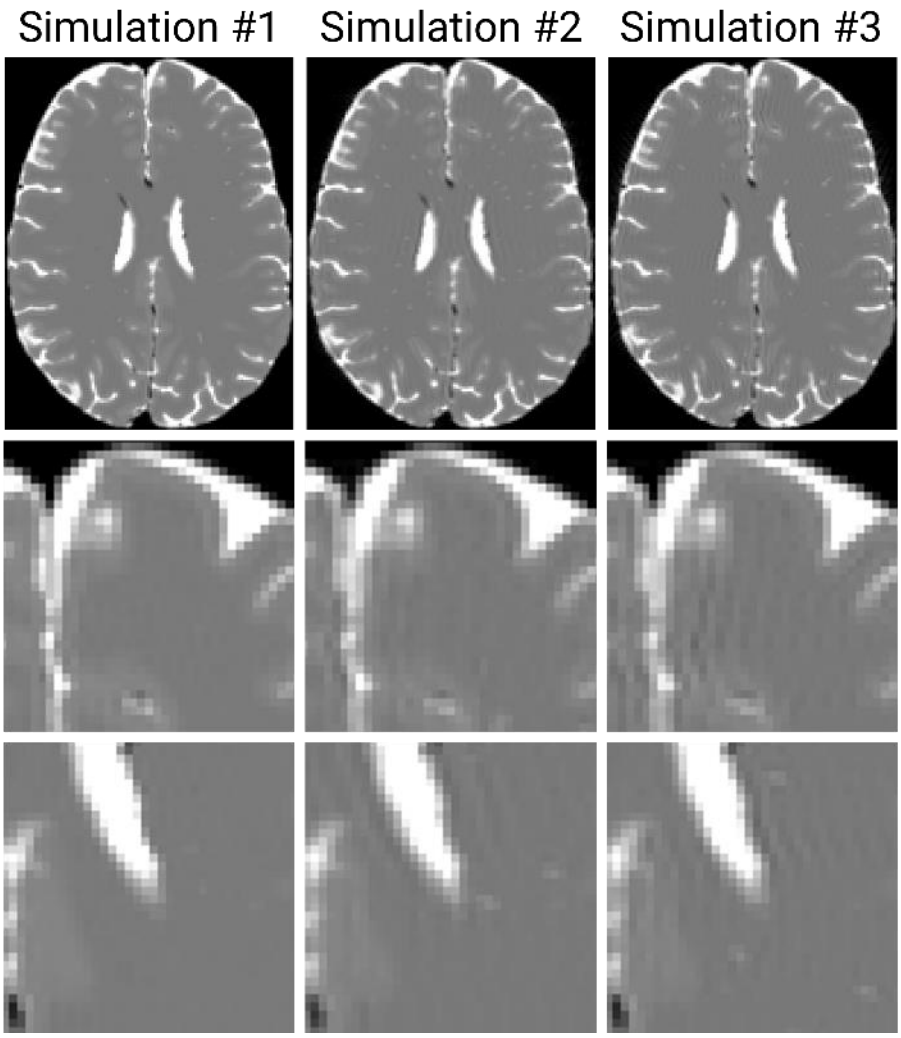

Figure 9. Motion causes ghosting artefacts, which could easily be confused with "tubular" structures. Imaging considerations: k-space sampling and motion artefacts.

We then gauged the effect motion artefacts could have on PVS segmentation to determine whether quantification was still feasible on motion corrupted scans (Figure 10). Motion caused variation in quantification. When visual artefacts were subtle, the performance was similar to that obtained after sampling. However, when these artefacts were evident (as in Figure 11), false positives were unavoidable for Hessian-based filters regardless of the considered threshold (max precision: Frangi: 86%; Jerman: 88%; RORPO: 100%) (Figure S2). This situation took place as ghosting or ringing artefacts caused by motion were detected as potential tubular structures (Figure 11).

Preprints (www.preprints.org) | NOT PEER-REVIEWED | Posted: 7 April 2022 doi:10.20944/preprints202204.0058.v1

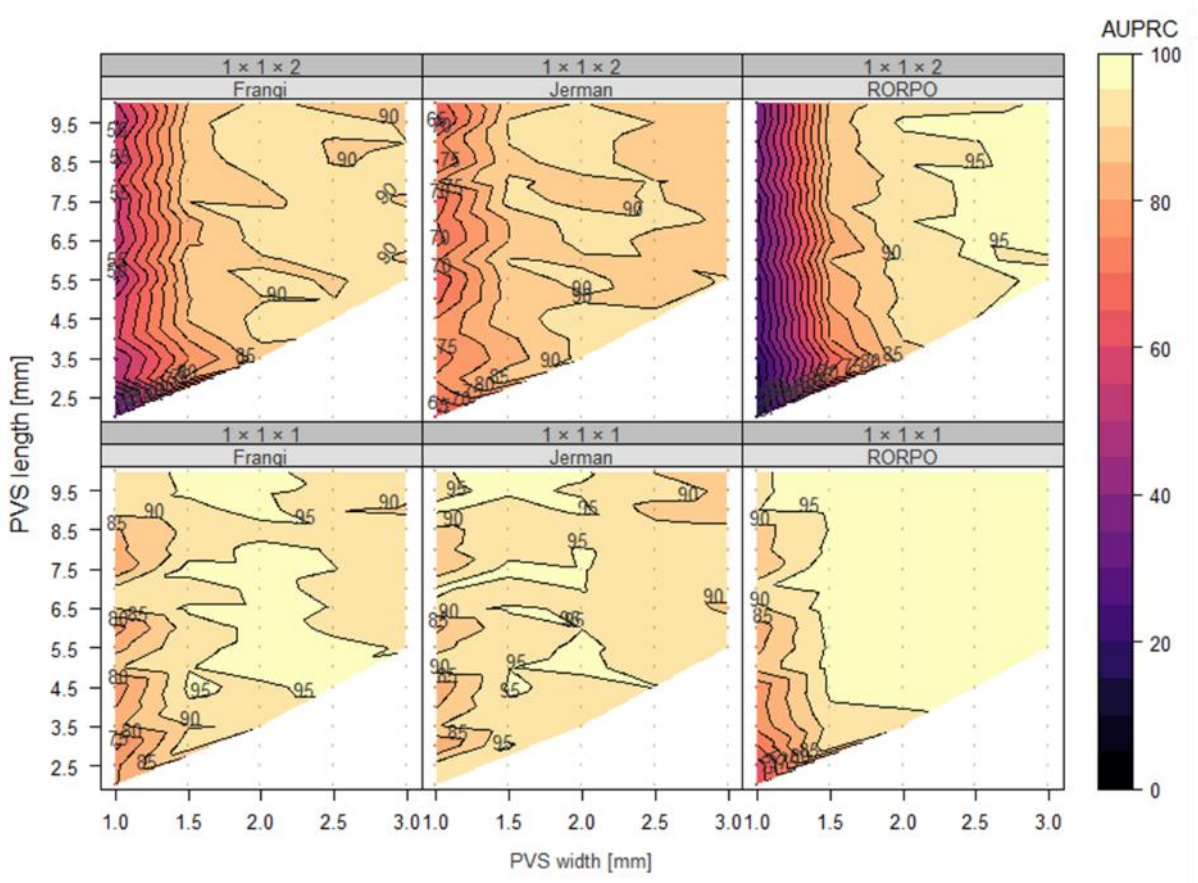

Figure 10. The performance of enhancement filters decreases with the presence of motion artefacts. We considered two scanning resolutions, 1 × 1 × 1 (bottom row) and 1 × 1 × 2 (top row) mm, to explore the impact of isotropic and anisotropic voxels on segmentation performance. White regions represent cases that were not considered (width >= length, eccentricity < 0.8, or lack of PVS visibility). Imaging considerations: k-space sampling and motion artefacts.

Preprints (www.preprints.org) | NOT PEER-REVIEWED | Posted: 7 April 2022 doi:10.20944/preprints202204.0058.v1

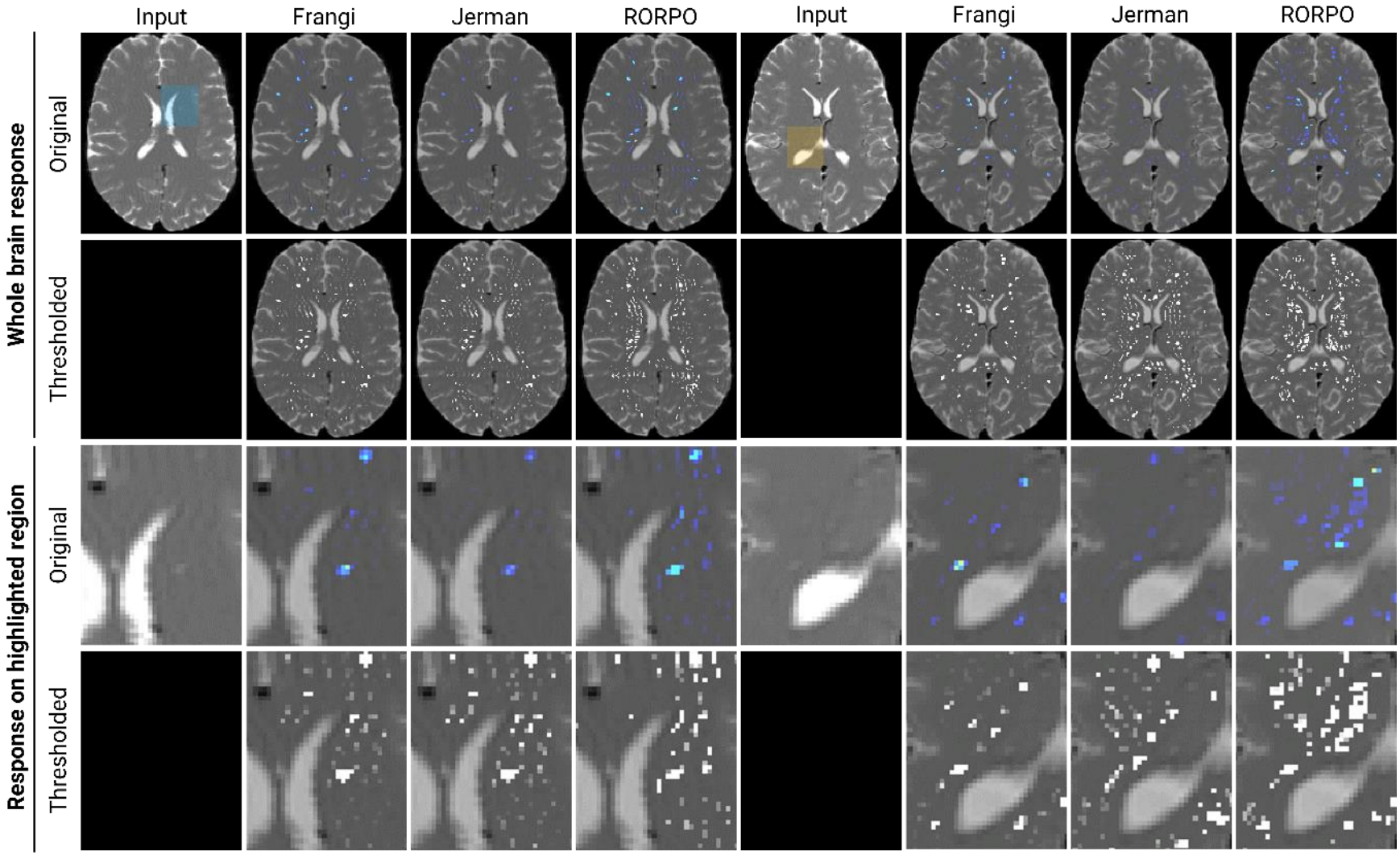

Figure 11. PVS enhancement filters detect ghosting artefacts caused by motion. We zoom in the blue and orange regions to illustrate problems further. Imaging considerations: k-space sampling and motion artefacts.

Preprints (www.preprints.org) | NOT PEER-REVIEWED | Posted: 7 April 2022 doi:10.20944/preprints202204.0058.v1

3.2.3 Rician noise

We incorporated Rician noise into the simulations to examine whether the level of noise present in the reference study (SNR = 7.14 [IQR 5.93, 8.43]) had any impact on the visibility and quantification of PVS. While PVS remained visible (Figure 12), Rician noise increased false positive rates (Figure 13), being particularly evident in images with anisotropic voxels (Figure S3). Among tested filters, the Jerman filter exhibited the highest AUPRC drop (Jerman: 3.11 [IQR 6.91, 2.52] vs Frangi: 1.55 [IQR 3.88, 1.18] and RORPO: 1.11 [IQR 2.06, 0.71]).

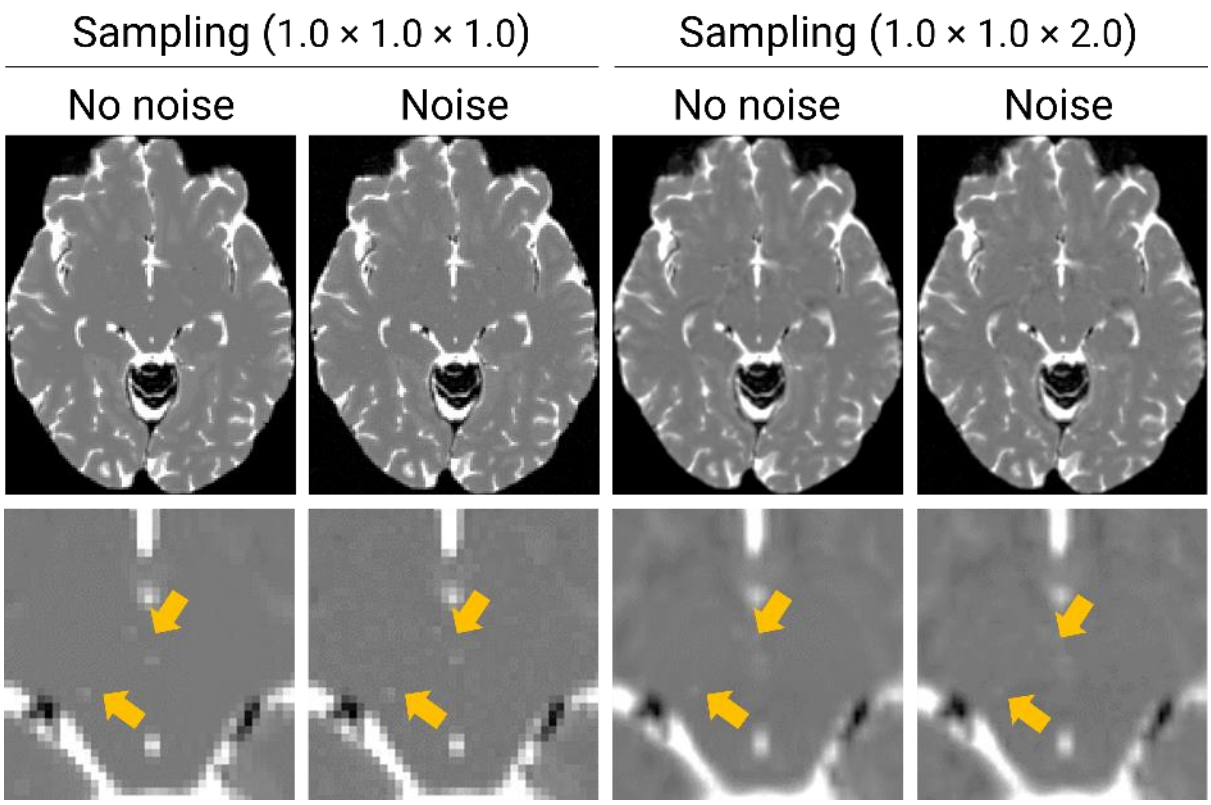

Figure 12. PVS remained visible after incorporating Rician noise into the simulations. Yellow arrows point to a few PVS. Spatiotemporal considerations: k-space sampling and noise. Imaging considerations: k-space sampling and Rician noise.

Preprints (www.preprints.org) | NOT PEER-REVIEWED | Posted: 7 April 2022 doi:10.20944/preprints202204.0058.v1

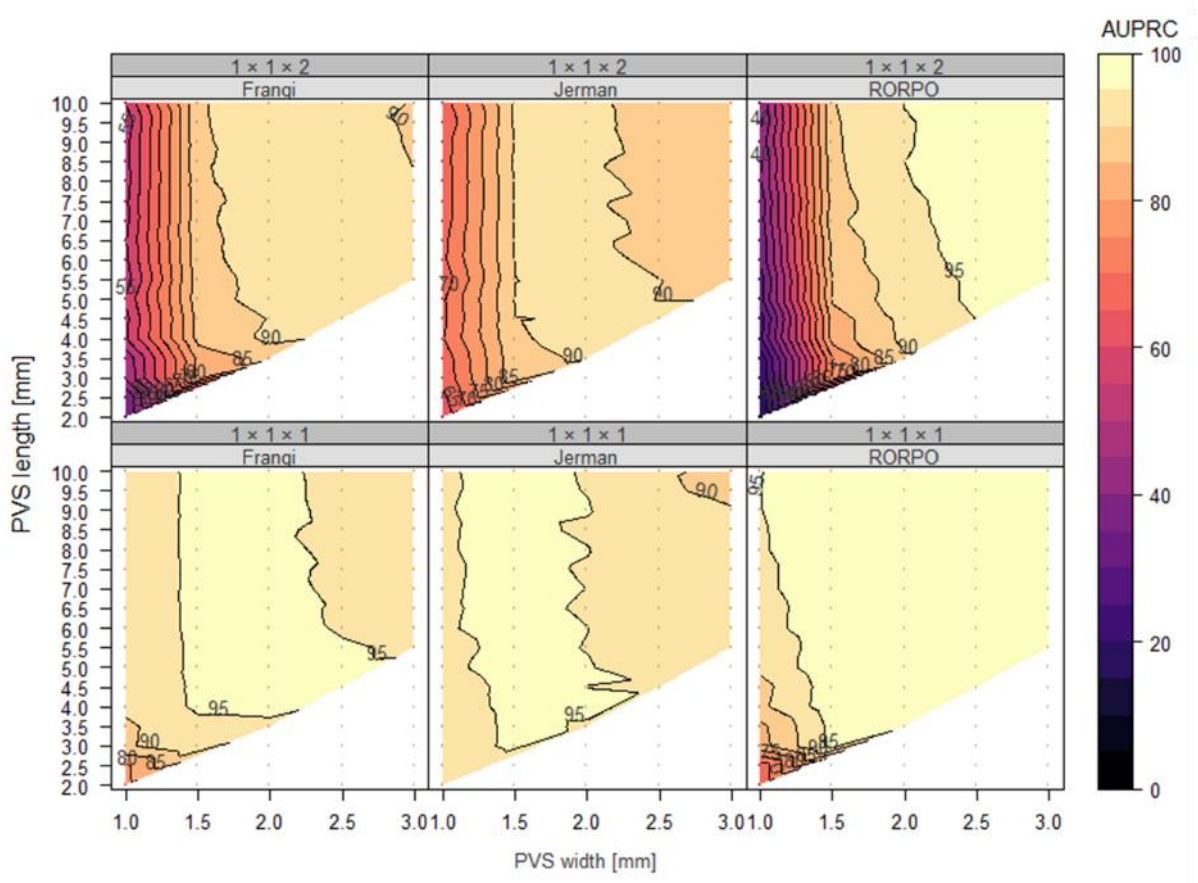

Figure 13. Enhancement filters are relatively robust to Rician noise. We consider two scanning resolutions, 1 × 1 × 1 (bottom row) and 1 × 1 × 2 (top row) mm, to explore the impact of isotropic and anisotropic voxels on segmentation performance. White regions represent cases that were not considered (width >= length, eccentricity < 0.8, or lack of PVS visibility). Imaging considerations: k-space sampling and Rician noise.

3.3 Effect of pathological regions

We synthesised WMH to determine whether enhancement filters can discern between hyperintense tubular and non-tubular structures (Figure 14). AUPRC values plummeted when we introduced WMH. For example, in 1 × 1 × 1 mm images, median values went from more than 90 to less than 75 (Frangi: from 94.21 [IQR 91.60, 96.16] to 43.76 [IQR 25.19, 63.38]; Jerman: from 94.51 [IQR 91.90, 95.37] to 58.00 [IQR 35.68, 64.87]; RORPO: from 98.72 [IQR 95.37, 98.96] to 71.87 [IQR 57.21, 76.63]). The zigzagging patterns seen in mean AUPRC plots (Figure 14) coincided with increased standard deviation in AUPRC values (Figure S5), suggesting it is only when PVS width surpasses 2 mm, when the response of a PVS and WMH starts to differ.

Preprints (www.preprints.org) | NOT PEER-REVIEWED | Posted: 7 April 2022 doi:10.20944/preprints202204.0058.v1

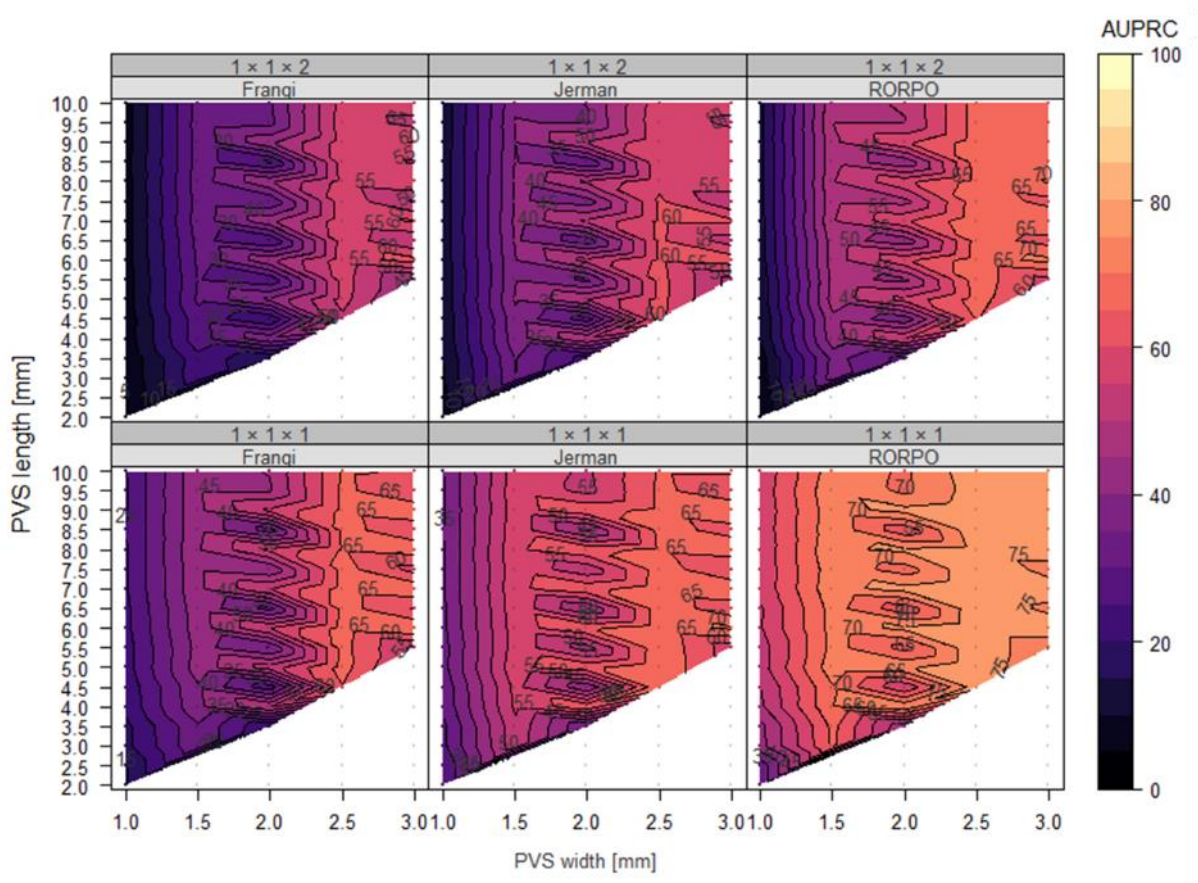

Figure 14. Enhancement filters cannot differentiate PVS from other hyperintense structures effectively. We consider two scanning resolutions, 1 × 1 × 1 (bottom row) and 1 × 1 × 2 (top row) mm, to explore the impact of isotropic and anisotropic voxels on segmentation performance. White regions represent cases that were not considered (width >= length, eccentricity < 0.8, or lack of PVS visibility). Imaging considerations: k-space sampling.

According to response maps, performance decline is a result of two factors (Figure 15). First, segmentation filters detect WMH either completely or partially – depending on their size. Second, contrast change due to overlap between PVS and WMH compromises the detection of PVS. We did not find a single threshold capable of separating WMH from PVS effectively. We also observed that only when PVS width is higher than 2 mm, the response of a PVS and WMH start to differ.

Preprints (www.preprints.org) | NOT PEER-REVIEWED | Posted: 7 April 2022 doi:10.20944/preprints202204.0058.v1

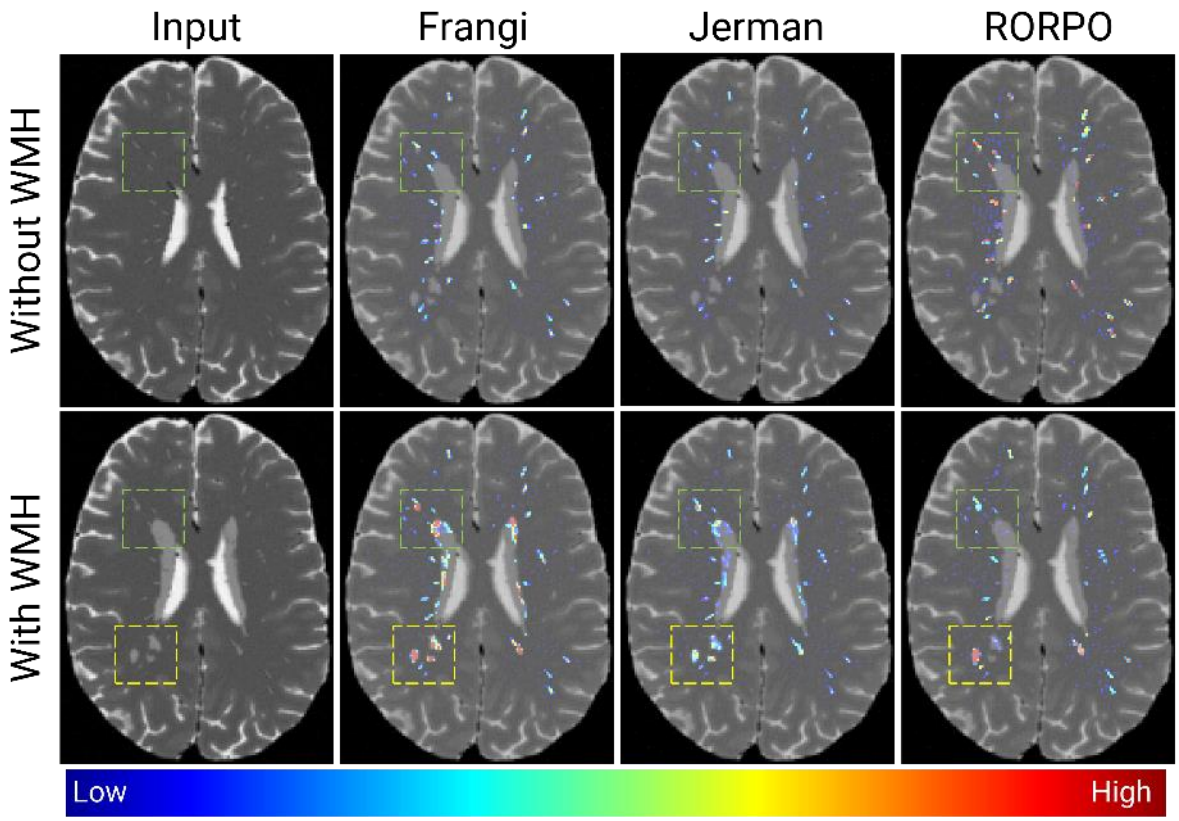

Figure 15. Response maps in the absence and presence of WMH (top and bottom row, respectively). Enhancement filters undesirably highlight WMH either partially or fully. Partial detections occur around boundaries of large WMH (green square) whereas full detection takes places when WMH appear as punctate foci (yellow square). Moreover, PVS are either completely missed or fragmented when PVS overlap with WMH (green square). Outputs cannot be compared between filters as values vary in range and scale.

4. Discussion

We presented a computational model for synthesising three-dimensional images with PVS-like structures to quantify the sensitivity and recall of PVS enhancement methods, particularly when images undergo distortion. With it, we detected key factors that influence PVS enhancement – ergo PVS quantification -- and that need to be taken into consideration to better measure PVS.

4.1 What enhancement method to use?

Briefly, the choice of one filter over another depends on whether researchers favour high true positive and false positive rates but low false negative rates (Frangi or Jerman) or the opposite (RORPO).

Two major drawbacks can also tip the balance one way or another. On the one hand, Hessian-based filters present poorer PVS localisation than RORPO, a consequence of the blurring that takes place before the computation of the Hessian matrix. This situation implies the maximum precision and recall

Preprints (www.preprints.org) | NOT PEER-REVIEWED | Posted: 7 April 2022 doi:10.20944/preprints202204.0058.v1

decrease as PVS size increases; PVS in close proximity will tend to be segmented as a single one; and segmentation errors around hyperintense regions other than PVS (e.g. lateral ventricles or WMH) are to be expected, unless these are perfectly excluded from the analyses. On the other hand, unlike Hessian-based filters, RORPO is unable to handle anisotropic voxels appropriately as it assumes distances between neighbouring voxels are constant in all directions.

Although a mixed approach – RORPO for isotropic voxels and Frangi for anisotropic voxels – would seem reasonable, we do not expect estimates yielded by these filters to be comparable: precision and recall vary depending on PVS dimensions and imaging conditions, and distributions of response map values vary in shape and scale.

4.2 Imaging artefacts lower precision rates

All visual distortions studied in this work reduced precision rates, irrespective of the filtering technique. Ringing due to *k*-space sampling or motion were the ones augmenting false positive rates the most, as these present a "tubular" shape. The RORPO filter was better at discerning between ringing artefacts and true PVS than the Frangi or Jerman filters, as response map values are associated with intensities – higher thresholds would thus separate very hyperintense objects from tubular objects.

PVS of certain dimensions stop being visible after *k*-space sampling. In 1 × 1 × 1 and 1 × 1 × 2 mm resolution images, PVS of length lower than 2 mm and width lower than 1 mm were simply not observable nor quantifiable. If potential PVS candidates with such dimensions were to be detected, it is reasonable to think they correspond to anything but a PVS. Connected component analysis may be useful to remove such noise.

4.3 The presence of other hyperintense lesions compromises PVS segmentation

The presence of WMH was particularly damaging for PVS quantification among all effects investigated in this study, as enhancement filters flagged them as potential PVS candidates. WMH thus boost false positive rates because their filter response values can be similar or greater than those of a PVS. The degree to which WMH are detected is determined on the size of the lesion and the filter. Tiny and focal WMH will be segmented completely, regardless of enhancement method. Hessian-based filters will detect the boundaries of large WMH whereas RORPO will disregard them and all PVS within them.

While our observations reflect the damaging effect of WMH on PVS segmentation, these problems can also occur with other hyperintense neuro-radiological features – e.g. ischaemic stroke lesions or lacunes, with wedged shapes or shapes similar to small WMH. Therefore, by synthesising WMH, and

Preprints (www.preprints.org) | NOT PEER-REVIEWED | Posted: 7 April 2022 doi:10.20944/preprints202204.0058.v1

evaluating the filters' ability to differentiate them from PVS, the confound that these other pathological features may pose for the accurate segmentation of PVS could be also estimated.

4.4 Implications

Our work has implications for the quantification of PVS on MRI. First, imaging artefacts have an impact on the sensitivity and precision of current segmentation methods. Thus, the development and validation of techniques to compensate for it during or after image acquisition is critical for measuring PVS. Second, the striking effect of hyperintense vascular lesions on PVS segmentation suggests that extremely careful – possibly manual -- delineation of these other lesions is needed to obtain actual estimates of PVS burden, e.g. mask the WMH first, then assess the PVS, but this will require visual inspection to differentiate PVS from WMH where the two coincide. Without these efforts, the final goal of understanding the involvement of PVS on brain health function and small vessel diseases on their own is simply not achievable as estimates will incorporate mixed effects. Third, correct binarisation remains a challenge as precision and recall rates, therefore "optimal" thresholds, vary with the quality of each individual scan. It is worth noting that by binarising "vesselness" response maps, we also increase the likelihood of splitting a single but tortuous PVS into multiple pieces as the response in its thin and thick segments would differ.

4.5 Limitations

Our computational model is limited by its assumptions and simplifications. First, our computational model does not mimic all acquisition processes. However, from a methodological standpoint, our research demonstrates spatiotemporal and imaging considerations influence PVS quantification and lays groundwork for future research. Our computational model might be used in conjunction with MRI simulators, such as MRilab (Liu et al., 2017), to enable testing and optimising imaging protocols for computational PVS assessments. Second, for the sake of simplicity, we assumed perivascular spaces could be represented as cylinders. Euclidean shapes nonetheless are unlikely representative of the actual curvilinear geometry of PVS observed in real life (see Fig. 2 in (Wardlaw et al., 2013)). Also, we limited out evaluations to some typical scenarios of imaging acquired under research protocols (e.g. slice thickness only of 0.5, 1 and 2 mm). More testing is required to establish the limits of validity of these methods (e.g., minimum length and width of PVS and spatial resolution requirements). Third, as highlighted in the introduction, we focused on the robustness of PVS enhancement methods rather than on the pre-processing and segmentation stages. Nonetheless, our computational model can be used to synthesise images "acquired" with multiple imaging protocols, head models, lesions and determine whether common processing techniques are suitable for these types of analyses.

 doi:10.20944/preprints202204.0058.v1

5. Conclusions

Our work reveals appropriate processing of MRI signals is necessary to maximise PVS measurement reliability. While enhancement filters can correctly facilitate identifying PVS, they are sensitive to imaging artefacts, such as ringing and motion, and ineffective at distinguishing between PVS from other hyperintense lesions of different shapes. These issues ultimately highlight the importance of masking out other neuroradiological features and of prospective or retrospective image enhancement for better PVS quantification. We have made our development publicly available for other researchers to build upon it and test their segmentation schemes in advance (https://github.com/joseabernal/PVSDRO.git).

6. CRediT authorship contribution statement

Jose Bernal: conceptualisation, methodology, software, formal analysis, investigation, writing – original draft preparation, writing – review and editing, visualisation. **Maria d. C. Valdés-Hernández**: patient study data collection, patient study data processing, resources, patient study data curation, writing – review and editing, supervision, funding acquisition, visualisation. **Javier Escudero**: resources, writing – review and editing, supervision, funding acquisition, visualisation. **Roberto Duarte**: methodology, software, writing – review and editing. **Lucia Ballerini:** patient study data collection, patient study data processing, methodology, software, writing – review and editing. **Mark E. Bastin**: patient study data collection, patient study data processing, study data curation, writing – review and editing. **Ian J. Deary:** funding acquisition, chief investigator of the patient study. **Michael J. Thrippleton**: software, methodology, writing – review and editing. **Rhian M. Touyz**: resources, writing – review and editing, supervision, funding acquisition. **Joanna M. Wardlaw**: resources, study data acquisition and curation, writing – review and editing, supervision, funding acquisition, project administration.

7. Conflict of interest

The authors declare no conflict of interest. The funders had no role in the design of the study; in the collection, analyses, or interpretation of data; in the writing of the manuscript, or in the decision to publish the results.

8. Acknowledgements

This work is supported by: MRC Doctoral Training Programme in Precision Medicine (JB - Award Reference No. 2096671); The Galen and Hilary Weston Foundation under the Novel Biomarkers 2019 scheme (ref UB190097) administered by the Weston Brain Institute; the UK Dementia Research

Institute which receives its funding from DRI Ltd, funded by the UK MRC, Alzheimer's Society and Alzheimer's Research UK; the Fondation Leducq Network for the Study of Perivascular Spaces in Small Vessel Disease (16 CVD 05); Stroke Association 'Small Vessel Disease-Spotlight on Symptoms (SVD-SOS)' (SAPG 19\100068); The Row Fogo Charitable Trust Centre for Research into Aging and the Brain (MVH) (BRO-D.FID3668413); British Heart Foundation Edinburgh Centre for Research Excellence (RE/18/5/34216); NHS Lothian Research and Development Office (MJT).

The LBC1936 study was funded by Age UK and the UK Medical Research Council (http://www.disconnectedmind.ed.ac.uk/) (including the Sidney De Haan Award for Vascular Dementia). LBC1936 MRI brain imaging was supported by Medical Research Council (MRC) grants G0701120, G1001245, MR/M013111/1 and MR/R024065/1. Funds were also received from The University of Edinburgh Centre for Cognitive Ageing and Cognitive Epidemiology, part of the cross council Lifelong Health and Wellbeing Initiative (MR/K026992/1), and the Biotechnology and Biological Sciences Research Council (BBSRC).

We thank the LBC1936 study participants, their families and radiographers at Edinburgh Imaging Facilities. We thank the LBC1936 study team members who recruited the participants of the study.

9. References

Ballerini, L., Booth, T., Valdés Hernández, M. del C., Wiseman, S., Lovreglio, R., Muñoz Maniega, S., Morris, Z., Pattie, A., Corley, J., Gow, A., Bastin, M.E., Deary, I.J., Wardlaw, J., 2020a. Computational quantification of brain perivascular space morphologies: Associations with vascular risk factors and white matter hyperintensities. A study in the Lothian Birth Cohort 1936. NeuroImage Clin. 25, 102120. https://doi.org/10.1016/j.nicl.2019.102120

Ballerini, L., Lovreglio, R., Valdés Hernández, M.D.C., Ramirez, J., MacIntosh, B.J., Black, S.E., Wardlaw, J.M., 2018. Perivascular Spaces Segmentation in Brain MRI Using Optimal 3D Filtering. Sci. Rep. 8, 1–11. https://doi.org/10.1038/s41598-018-19781-5

Ballerini, L., McGrory, S., Valdés Hernández, M. del C., Lovreglio, R., Pellegrini, E., MacGillivray, T., Muñoz Maniega, S., Henderson, R., Taylor, A., Bastin, M.E., Doubal, F., Trucco, E., Deary, I.J., Wardlaw, J., 2020b. Quantitative measurements of enlarged perivascular spaces in the brain are associated with retinal microvascular parameters in older community-dwelling subjects. Cereb. Circ. - Cogn. Behav. 1, 100002. https://doi.org/10.1016/j.cccb.2020.100002

Bernal, J., Valdés-Hernández, M. d. C., Escudero, J., Heye, A.K., Sakka, E., Armitage, P.A., Makin, S., Touyz, R.M., Wardlaw, J.M., Thrippleton, M.J., 2021a. A four-dimensional computational model of dynamic contrast-enhanced magnetic resonance imaging measurement of subtle blood-brain barrier leakage. Neuroimage 230, 117786. https://doi.org/10.1016/j.neuroimage.2021.117786

Bernal, J., Xu, W., Valdés-Hernández, M. d. C., Escudero, J., Jochems, A.C.C., Clancy, U., Doubal, F.N., Stringer, M.S., Thrippleton, M.J., Touyz, R.M., Wardlaw, J.M., 2021b. Selective Motion Artefact Reduction via Radiomics and k-space Reconstruction for Improving Perivascular Space Quantification in Brain Magnetic Resonance Imaging, Lecture Notes in Computer Science (including subseries Lecture Notes in Artificial Intelligence and Lecture Notes in Bioinformatics).

Springer International Publishing. https://doi.org/10.1007/978-3-030-80432-9_12

Deary, I.J., Gow, A.J., Taylor, M.D., Corley, J., Brett, C., Wilson, V., Campbell, H., Whalley, L.J., Visscher, P.M., Porteous, D.J., Starr, J.M., 2007. The Lothian Birth Cohort 1936: A study to examine influences on cognitive ageing from age 11 to age 70 and beyond. BMC Geriatr. 7, 1–12. https://doi.org/10.1186/1471-2318-7-28

Francis, F., Ballerini, L., Wardlaw, J.M., 2019. Perivascular spaces and their associations with risk factors, clinical disorders and neuroimaging features: A systematic review and meta-analysis. Int. J. Stroke 14, 359–371. https://doi.org/10.1177/1747493019830321

Frangi, A.F., Niessen, W.J., Vincken, K.L., Viergever, M.A., 1998. Multiscale vessel enhancement filtering 130–137. https://doi.org/10.1007/BFb0056195

González-Castro, V., Valdés Hernández, M. del C., Chappell, F.M., Armitage, P.A., Makin, S., Wardlaw, J.M., 2017. Reliability of an automatic classifier for brain enlarged perivascular spaces burden and comparison with human performance. Clin. Sci. 131, 1465–1481. https://doi.org/10.1042/CS20170051

Heier, L.A., Bauer, C.J., Schwartz, L., Zimmerman, R.D., Morgello, S., Deck, M.D.F., 1987. Large Virchow-Robin Spaces : MR-Ciinical Correlation 20, 929–936.

Heijmans, H., Buckley, M., Talbot, H., 2005. Path openings and closings. J. Math. Imaging Vis. 22, 107–119. https://doi.org/10.1007/s10851-005-4885-3

Iacono, M.I., Neufeld, E., Akinnagbe, E., Bower, K., Wolf, J., Oikonomidis, I.V., Sharma, D., Lloyd, B., Wilm, B.J., Wyss, M., Pruessmann, K.P., Jakab, A., Makris, N., Cohen, E.D., Kuster, N., Kainz, W., Angelone, L.M., 2015. MIDA: A multimodal imaging-based detailed anatomical model of the human head and neck. PLoS One 10. https://doi.org/10.1371/journal.pone.0124126

Jerman, T., Pernuš, F., Likar, B., Špiclin, Ž., 2015. Beyond Frangi: an improved multiscale vesselness filter. Med. Imaging 2015 Image Process. 9413, 94132A. https://doi.org/10.1117/12.2081147

Lamy, J., Merveille, O., Kerautret, B., Passat, N., Lamy, J., Merveille, O., Kerautret, B., Passat, N., Vesselness, A.V., Lamy, J., 2020. Vesselness filters : A survey with benchmarks applied to liver imaging, in: International Conference on Pattern Recognition.

Li, Y., Li, M., Zuo, L., Shi, Q., Qin, W., Yang, L., Jiang, T., Hu, W., 2018. Compromised blood-brain barrier integrity is associated with total magnetic resonance imaging burden of cerebral small vessel disease. Front. Neurol. 9. https://doi.org/10.3389/fneur.2018.00221

Liu, C., Habib, T., Salimeen, M., Pradhan, A., Singh, M., Wang, M., Wu, F., Zhang, Y., Gao, L., Yang, G., Li, X., Yang, J., 2020. Quantification of visible Virchow–Robin spaces for detecting the functional status of the glymphatic system in children with newly diagnosed idiopathic generalized epilepsy. Seizure 78, 12–17. https://doi.org/10.1016/j.seizure.2020.02.015

Liu, F., Velikina, J. V., Block, W.F., Kijowski, R., Samsonov, A.A., 2017. Fast Realistic MRI Simulations Based on Generalized Multi-Pool Exchange Tissue Model. IEEE Trans. Med. Imaging 36, 527–537. https://doi.org/10.1109/TMI.2016.2620961

Merveille, O., Talbot, H., Najman, L., Passat, N., 2018. Curvilinear Structure Analysis by Ranking the Orientation Responses of Path Operators. IEEE Trans. Pattern Anal. Mach. Intell. 40, 304–317. https://doi.org/10.1109/TPAMI.2017.2672972

Merveille, O., Talbot, H., Najman, L., Passat, N., 2014. Tubular structure filtering by ranking orientation responses of path operators. Lect. Notes Comput. Sci. (including Subser. Lect. Notes Artif. Intell. Lect. Notes Bioinformatics) 8690 LNCS, 203–218. https://doi.org/10.1007/978-3-319-10605-

2_14

Patankar, T.F., Mitra, D., Varma, A., Snowden, J., Neary, D., Jackson, A., 2005. Dilatation of the Virchow-Robin space is a sensitive indicator of cerebral microvascular disease: Study in elderly patients with dementia. Am. J. Neuroradiol. 26, 1512–1520.

Pierpaoli, C., Basser, P.J., 1996. Toward a quantitative assessment of diffusion anisotropy. Magn. Reson. Med. 36, 893–906. https://doi.org/10.1002/mrm.1910360612

Potter, G.M., Chappell, F.M., Morris, Z., Wardlaw, J.M., 2015. Cerebral perivascular spaces visible on magnetic resonance imaging: Development of a qualitative rating scale and its observer reliability. Cerebrovasc. Dis. 39, 224–231. https://doi.org/10.1159/000375153

Ramirez, J., Berezuk, C., McNeely, A.A., Scott, C.J.M., Gao, F., Black, S.E., 2015. Visible Virchow-Robin spaces on magnetic resonance imaging of Alzheimer's disease patients and normal elderly from the Sunnybrook dementia study. J. Alzheimer's Dis. 43, 415–424. https://doi.org/10.3233/JAD-132528

Rouhl, R.P.W., Van Oostenbrugge, R.J., Knottnerus, I.L.H., Staals, J.E.A., Lodder, J., 2008. Virchow-Robin spaces relate to cerebral small vessel disease severity. J. Neurol. 255, 692–696. https://doi.org/10.1007/s00415-008-0777-y

Sepehrband, F., Barisano, G., Sheikh-Bahaei, N., Cabeen, R.P., Choupan, J., Law, M., Toga, A.W., 2019. Image processing approaches to enhance perivascular space visibility and quantification using MRI. Sci. Rep. 9, 1–12. https://doi.org/10.1038/s41598-019-48910-x

Sepehrband, F., Barisano, G., Sheikh-bahaei, N., Cabeen, R.P., Lynch, K.M., Crawford, M.S., Lan, H., 2021. Volumetric Distribution of Perivascular Space in Relation to Mild Cognitive Impairment. Neurobiol. Aging 99, 28–43. https://doi.org/10.1016/j.neurobiolaging.2020.12.010.Volumetric

Shaw, R., Sudre, C.H., Varsavsky, T., Ourselin, S., Cardoso, M.J., 2020. A k-Space Model of Movement Artefacts: Application to Segmentation Augmentation and Artefact Removal. IEEE Trans. Med. Imaging 0062, 1–1. https://doi.org/10.1109/tmi.2020.2972547

Valdés Hernández, M. del C., Ballerini, L., Glatz, A., Muñoz Maniega, S., Gow, A.J., Bastin, M.E., Starr, J.M., Deary, I.J., Wardlaw, J.M., 2020. Perivascular spaces in the centrum semiovale at the beginning of the 8th decade of life: effect on cognition and associations with mineral deposition. Brain Imaging Behav. 14, 1865–1875. https://doi.org/10.1007/s11682-019-00128-1

Vilanova, A., Zhang, S., Kindlmann, G., Laidlaw, D., 2006. An introduction to visualization of diffusion tensor imaging and its applications. Math. Vis. 0, 121–153. https://doi.org/10.1007/3-540-31272-2_7

Wang, X., Chappell, F.M., Valdes Hernandez, M., Lowe, G., Rumley, A., Shuler, K., Doubal, F., Wardlaw, J.M., 2016. Endothelial Function, Inflammation, Thrombosis, and Basal Ganglia Perivascular Spaces in Patients with Stroke. J. Stroke Cerebrovasc. Dis. 25, 2925–2931. https://doi.org/10.1016/j.jstrokecerebrovasdis.2016.08.007

Wardlaw, J.M., Benveniste, H., Nedergaard, M., Zlokovic, B. V., Mestre, H., Lee, H., Doubal, F.N., Brown, R., Ramirez, J., MacIntosh, B.J., Tannenbaum, A., Ballerini, L., Rungta, R.L., Boido, D., Sweeney, M., Montagne, A., Charpak, S., Joutel, A., Smith, K.J., Black, S.E., 2020. Perivascular spaces in the brain: anatomy, physiology and pathology. Nat. Rev. Neurol. 16, 137–153. https://doi.org/10.1038/s41582-020-0312-z

Wardlaw, J.M., Smith, E.E., Biessels, G.J., Cordonnier, C., Fazekas, F., Frayne, R., Lindley, R.I., O'Brien, J.T., Barkhof, F., Benavente, O.R., Black, S.E., Brayne, C., Breteler, M., Chabriat, H., DeCarli, C., de Leeuw, F.E., Doubal, F., Duering, M., Fox, N.C., Greenberg, S., Hachinski, V., Kilimann, I., Mok, V.,

 doi:10.20944/preprints202204.0058.v1

Oostenbrugge, R. van, Pantoni, L., Speck, O., Stephan, B.C.M., Teipel, S., Viswanathan, A., Werring, D., Chen, C., Smith, C., van Buchem, M., Norrving, B., Gorelick, P.B., Dichgans, M., 2013. Neuroimaging standards for research into small vessel disease and its contribution to ageing and neurodegeneration. Lancet Neurol. 12, 822–838. https://doi.org/10.1016/S1474-4422(13)70124-8